

# Nonlinear synthesis of infrasound propagation through an inhomogeneous, absorbing atmosphere

C. D. de Groot-Hedlin<sup>a)</sup>

*Institute of Geophysics and Planetary Physics, Scripps Institution of Oceanography, La Jolla, California 92093-0225*

(Received 10 January 2012; revised 5 May 2012; accepted 12 June 2012)

An accurate and efficient method to predict infrasound amplitudes from large explosions in the atmosphere is required for diverse source types, including bolides, volcanic eruptions, and nuclear and chemical explosions. A finite-difference, time-domain approach is developed to solve a set of nonlinear fluid dynamic equations for total pressure, temperature, and density fields rather than acoustic perturbations. Three key features for the purpose of synthesizing nonlinear infrasound propagation in realistic media are that it includes gravitational terms, it allows for acoustic absorption, including molecular vibration losses at frequencies well below the molecular vibration frequencies, and the environmental models are constrained to have axial symmetry, allowing a three-dimensional simulation to be reduced to two dimensions. Numerical experiments are performed to assess the algorithm's accuracy and the effect of source amplitudes and atmospheric variability on infrasound waveforms and shock formation. Results show that infrasound waveforms steepen and their associated spectra are shifted to higher frequencies for nonlinear sources, leading to enhanced infrasound attenuation. Results also indicate that nonlinear infrasound amplitudes depend strongly on atmospheric temperature and pressure variations. The solution for total field variables and insertion of gravitational terms also allows for the computation of other disturbances generated by explosions, including gravity waves. © 2012 Acoustical Society of America. [<http://dx.doi.org/10.1121/1.4731468>]

PACS number(s): 43.25.Cb, 43.28.Js, 43.25.Ed [DKW]

Pages: 646–656

## I. INTRODUCTION

Explosions that occur in the atmosphere are immense sources of infrasound energy (acoustic energy below 20 Hz, the limit of human hearing) that can be detected at distances of hundreds to thousands of kilometers from the source. The high efficiency of infrasound propagation is due to two characteristics of the Earth's atmosphere. First, the intrinsic absorption of sound energy in air varies approximately as the square of the frequency (Sutherland and Bass, 2004; de Groot-Hedlin, 2008) so that infrasound is attenuated much less than audible sounds. Only at altitudes above the stratopause, at about 50 km, is the molecular density low enough to cause significant attenuation at infrasonic frequencies (Sutherland and Bass, 2004). Second, both the air temperature (which is proportional to the square of the static sound speed) and winds are highly stratified, such that infrasound energy is ducted between the ground, where it is reflected, and sound and wind speed gradients at higher altitudes, where it is refracted back to the Earth (e.g., Evers and Haak, 2010, and references therein).

The fact that explosions in the atmosphere generate enormous acoustic signals, combined with the efficiency of low frequency acoustic transmission, has led to the use of infrasound in estimating source yield for nuclear (Mutschlecner and Whitaker, 2010; Gainville *et al.*, 2010) and chemical

(Bhattacharyya *et al.*, 2003; Whitaker *et al.*, 2003; Mutschlecner and Whitaker, 2010) explosions, and for constraining the kinetic energy released by meteoroid explosions (Edwards *et al.*, 2004; Edwards *et al.*, 2006; Le Pichon *et al.*, 2008). In fact, the value of infrasound for constraining source yield has led to the deployment of a global network of micro-barometers to aid in monitoring compliance with the Comprehensive Nuclear-Test-Ban Treaty (Christie and Campus, 2010). Current methods of estimating the size of a source from infrasound data make use of empirical formulations that predict pressure amplitude, based on a combination of factors including the source yield, the source–receiver range, and wind speed values derived from climate models. These formulations are derived from infrasound data from a series of atmospheric nuclear tests conducted at the Nevada Test Site in the 1950s (Mutschlecner and Whitaker, 2010, and references therein) and from high explosive tests conducted between 1981 and 2002 (Mutschlecner and Whitaker, 2010; Gainville *et al.*, 2010). These recordings showed that infrasound pressure amplitude from large explosions, corrected for the effect of stratospheric winds, decreases more rapidly than for spherical spreading, as would be expected if the propagation were purely linear.

It is necessary to advance our understanding of nonlinear infrasound propagation through realistic models of the atmosphere to develop better methods of estimating source yields from infrasound recordings. Nonlinear acoustic propagation implies that the amplitude of the pressure perturbation due to the passage of the sound wave is a significant fraction

<sup>a)</sup>Author to whom correspondence should be addressed. Electronic mail: [chedlin@ucsd.edu](mailto:chedlin@ucsd.edu)

of the ambient pressure. Of most significance to source yield studies is the fact that, for nonlinear propagation, a doubling of source size does not necessarily imply a doubling of recorded pressure for identical atmospheric conditions, whereas for the case of linear propagation it does. One hypothesis to explain the observation that the infrasound pressure generated by large explosions decreases more rapidly than for spherical spreading is that nonlinear acoustic propagation shifts energy from lower to higher frequencies, which are then preferentially attenuated, leading to a higher absorption of sound (Bass *et al.*, 2006). Other studies indicate that infrasound amplitudes from explosions depend mainly on atmospheric winds and temperature (e.g., Gainville *et al.*, 2010). A full description of nonlinear infrasound propagation requires precise atmospheric models that account for variability in wind speeds and temperature (Drob *et al.*, 2003) as well as attenuation (Sutherland and Bass, 2004). Computational methods that have been applied to time-domain modeling of nonlinear infrasound propagation from explosive sources include a weakly nonlinear approach performed on a three-dimensional (3D) Cartesian grid (del Pino *et al.*, 2009) and a shock-capturing filtering approach performed on a two-dimensional (2D) Cartesian grid (Marsden *et al.*, 2008). Both methods rely on the discretization of equations governing the acoustic propagation, however neither method incorporates atmospheric absorption.

The objective of this study is to examine nonlinear infrasound propagation for cylindrically symmetric sources embedded in realistic atmospheric models. A computationally efficient algorithm to synthesize the effect of shock wave propagation through an absorbing atmosphere with variable temperature and pressure is developed and presented. The method is similar to algorithms found in Wochner *et al.* (2005) and Shepherd *et al.* (2009), which accurately synthesize nonlinear acoustic propagation for high frequency acoustics and include the effects of dominant atmospheric attenuation mechanisms, including absorption due to shear and bulk viscosity, thermal conductivity, and molecular vibration. There are three key differences to the algorithm presented here: It allows for molecular vibration losses at frequencies well below molecular vibration frequencies; gravitational terms are included in the governing equations; and nonlinear fluid dynamic equations governing acoustic propagation are expanded in an axisymmetric cylindrical coordinate system, rather than a Cartesian (Wochner *et al.*, 2005) or spherical coordinate system (Shepherd *et al.*, 2009). The use of an axisymmetric cylindrical coordinate system is significant for this application in that an accurate and computationally efficient method of computing infrasound propagation from a 3D source embedded in an atmospheric model with realistic variations in ambient pressure and temperature can be achieved through the use of a 2D coordinate system. However, it also implies that the assumed atmospheric model is axisymmetric, so that out-of-plane acoustic propagation is not modeled.

The paper is structured as follows: In Sec. II, a computationally efficient method of solving the equations governing nonlinear infrasound propagation through a realistic atmosphere is presented. The governing equations are expanded in

cylindrical coordinates, with the inclusion of gravitational terms. Because the frequencies of interest to infrasound propagation are typically far below the molecular relaxation frequencies of nitrogen and oxygen—the dominant molecular constituents of the atmosphere—a low frequency approximation (Pierce, 1981) to molecular relaxation effects is applied. In Sec. III, several numerical examples are presented to demonstrate the accuracy of the method for simple models, and to show how infrasound amplitudes vary with range, source magnitude, and atmospheric variability. It is also shown that different source types, i.e., mass sources vs thermal sources, affect the partitioning of energy between blast waves and other atmospheric residuals near the source region. The paper concludes with remarks on the implications of the results for nuclear monitoring, and future improvements to the algorithm.

## II. NUMERICAL SOLUTION OF NONLINEAR INFRASOUND PROPAGATION

The fluid dynamic equations that describe the physics of nonlinear acoustic propagation in a realistic atmospheric model, including the effects of viscosity, thermal conductivity, and molecular vibration losses, are described here. More details may be found in Landau and Lifshitz (1959), Pierce (1981), and Wochner *et al.* (2005). The equations are the continuity equation,

$$\frac{\partial \rho}{\partial t} = -\nabla \cdot (\rho \vec{v}), \quad (1)$$

the Navier–Stokes equation,

$$\rho \frac{D\vec{v}}{Dt} = -\nabla p - \rho \vec{g} + \mu \nabla^2 \vec{v} + (\mu_B + \mu/3) \nabla(\nabla \cdot \vec{v}) \quad (2)$$

(e.g., Eq. 15.6 of Landau and Lifshitz, 1959), the entropy balance equation,

$$\rho \frac{DS_{fr}}{Dt} = -\sum_n \frac{\rho}{T_n} c_{vn} \frac{DT_n}{Dt} + \nabla \cdot \left( \frac{\kappa}{T} \nabla T \right) + \sigma_s \quad (3)$$

(Eq. 10-7.20 of Pierce, 1981), where

$$\frac{DT_n}{Dt} = \frac{1}{\tau_n} (T - T_n) \quad (4)$$

is the molecular relaxation equation. Equation (4) applies to each molecular constituent of the air; only nitrogen and oxygen are considered in this study.

In the above-presented equations,  $\rho$  denotes the density,  $\vec{v}$  the particle velocity,  $t$  the time,  $p$  the pressure,  $\mu$  and  $\mu_B$  are the shear and bulk viscosities,  $\vec{g}$  is the gravity vector, equal to  $[0, 0, 9.8 \text{ m/s}^2]$ ,  $S_{fr}$  is the entropy that would result if the vibrational degrees of freedom of the air molecules were frozen,  $\kappa$  is the thermal conductivity coefficient,  $T$  is the temperature,  $T_n$  and  $\tau_n$  are the vibrational temperature and relaxation time of the  $n$ th-type molecule,  $c_{vn}$  is the specific

heat at constant volume for the  $n$ th-type molecule, and  $\sigma_s$  denotes an entropy source term.

The gravitational term  $-\rho\vec{g}$  in Eq. (2) is not included in studies that deal with shock waves at higher frequencies (e.g., [Wochner et al., 2005](#); [Shepherd et al., 2009](#)), but is needed at infrasound frequencies to incorporate the decrease in ambient atmospheric pressure and density with altitude due to gravity. At frequencies well above the Brunt–Väisälä frequency (also called the buoyancy or stability frequency), which ranges from about 2 to 5 mHz for typical atmospheric temperature profiles ([Lingeitch et al., 1999](#)), this term may be neglected only if the pressure gradient term in Eq. (2) is replaced by  $\nabla(p - p_0)$ , where  $p_0$  is the ambient pressure. Since shear attenuation terms are very small compared to other attenuating mechanisms, the  $\mu\nabla^2\vec{v}$  and  $(\mu_B + \mu/3)\nabla(\nabla \bullet \vec{v})$  terms within the Navier–Stokes equations are approximated by a single  $\mu_t\nabla^2\vec{v}$  term, where  $\mu_t = \mu_B + 4/3\mu$ , for the remainder of this paper.

Expressions are required for the temperature and gas pressure to complete the set of governing equations. As in [Wochner et al. \(2005\)](#), temperature is given by

$$T = T_0(\rho/\rho_0)^{\gamma-1} \exp((\gamma-1)(S_{\text{fr}} - S_{\text{fr}0})/R_a), \quad (5)$$

where  $T_0$  is the ambient atmospheric temperature,  $\rho_0$  the ambient atmospheric density, the specific heat ratio,  $\gamma$ , is equal to 1.4 for air, and the specific gas constant,  $R_a$ , has a value of  $287.05 \text{ J kg}^{-1} \text{ K}^{-1}$ . This expression for temperature may be derived from entropy relations for an ideal gas. The pressure is then derived from the equation of state; the ideal gas law is used in this study,

$$p = \rho R_a T. \quad (6)$$

One of the challenges of modeling nonlinear infrasound propagation is that absolute pressure and particle velocities are required for computation, therefore methods that synthesize propagation through 3D media are required. However, a fully 3D method is prohibitive in terms of the high central processing unit time and storage required for most applications. A practical shortcut is to adopt an axially symmetric model so that, by employing a cylindrical coordinate frame, infrasound waveforms may be synthesized using only two spatial dimensions. This allows for synthesis of acoustic propagation on a desktop computer for axisymmetric models.

Following [Wochner et al. \(2005\)](#) and [Shepherd et al. \(2009\)](#), nonlinear solutions are derived for total field variables by recasting the above-presented constitutive equations in conservative form. Solving for total field variables in this way allows for the computation of all disturbances resulting from a given source, rather than only the acoustical components of the fields. Expansion of the governing equations in conservative form, in cylindrical coordinates, leads to the following set of equations for  $r \neq 0$ .

The equation for the conservation of mass becomes

$$\frac{\partial \rho}{\partial t} = -\frac{\partial(\rho v_r)}{\partial r} - \frac{\partial(\rho v_z)}{\partial z} - \frac{\rho v_r}{r}. \quad (7)$$

The Navier–Stokes equations become

$$\begin{aligned} \frac{\partial(\rho v_r)}{\partial t} = & -\frac{\partial}{\partial r}(p + \rho v_r^2) - \frac{\partial}{\partial z}(\rho v_r v_z) - \frac{\rho v_r^2}{r} \\ & + \mu_t \left( \frac{\partial^2}{\partial r^2} + \frac{1}{r} \frac{\partial}{\partial r} - \frac{1}{r^2} + \frac{\partial^2}{\partial z^2} \right) v_r \end{aligned} \quad (8a)$$

and

$$\begin{aligned} \frac{\partial(\rho v_z)}{\partial t} = & -\frac{\partial}{\partial r}(\rho v_z v_r) - \frac{\partial}{\partial z}(p + \rho v_z^2) - \rho g - \frac{\rho v_z v_r}{r} \\ & + \mu_t \left( \frac{\partial^2}{\partial r^2} + \frac{1}{r} \frac{\partial}{\partial r} + \frac{\partial^2}{\partial z^2} \right) v_z, \end{aligned} \quad (8b)$$

where  $g = 9.8 \text{ m/s}^2$ . The entropy balance equation becomes

$$\begin{aligned} \frac{\partial(\rho S_{\text{fr}})}{\partial t} = & -\frac{\partial}{\partial r}(\rho S_{\text{fr}} v_r) - \frac{\partial}{\partial z}(\rho S_{\text{fr}} v_z) - \frac{\rho S_{\text{fr}} v_r}{r} \\ & - \sum_n \frac{c_{vn}}{T_n} \frac{D(\rho T_n)}{Dt} \\ & + \left[ \frac{\partial}{\partial r} \left( \frac{\kappa}{T} \frac{\partial}{\partial r} \right) + \frac{\kappa}{rT} \frac{\partial}{\partial r} + \frac{\partial}{\partial z} \left( \frac{\kappa}{T} \frac{\partial}{\partial z} \right) \right] T + \sigma_s, \end{aligned} \quad (9)$$

and

$$\begin{aligned} \frac{\partial(\rho T_n)}{\partial t} = & -\frac{\partial}{\partial r}(\rho v_r T_n) - \frac{\partial}{\partial z}(\rho v_z T_n) - \frac{\rho T_n v_r}{r} \\ & + \frac{1}{\tau_n} (T - T_n). \end{aligned} \quad (10)$$

The governing equations, Eqs. (7)–(10), can be expressed more compactly in matrix form as

$$\frac{\partial \vec{F}}{\partial t} + \frac{\partial \vec{A}}{\partial r} + \frac{\partial \vec{B}}{\partial z} = \vec{H} + \vec{C}, \quad (11)$$

where  $\vec{F}$  are the time dependent field variables, and the radial and vertical derivatives act upon the  $\vec{A}$  and  $\vec{B}$  matrices, respectively. Source-like terms are split into two matrices,  $\vec{C}$  and  $\vec{H}$ , where terms in  $\vec{C}$  are nonzero in cylindrical coordinates and zero for a system reduced to 2D Cartesian coordinates, and  $\vec{H}$  comprises the remainder of the source-like terms. The matrices  $\vec{F}$ ,  $\vec{A}$ ,  $\vec{B}$ , and  $\vec{H}$  are defined as follows:

$$\vec{F} = \begin{pmatrix} \rho \\ \rho v_r \\ \rho v_z \\ \rho S_{\text{fr}} \\ \rho T_{\text{N}_2} \\ \rho T_{\text{O}_2} \end{pmatrix}, \quad \vec{A} = \begin{pmatrix} \rho v_r \\ p + \rho v_r^2 \\ \rho v_r v_z \\ \rho v_r S_{\text{fr}} \\ \rho v_r T_{\text{N}_2} \\ \rho v_r T_{\text{O}_2} \end{pmatrix}, \quad \vec{B} = \begin{pmatrix} \rho v_z \\ \rho v_r v_z \\ p + \rho v_z^2 \\ \rho v_z S_{\text{fr}} \\ \rho v_z T_{\text{N}_2} \\ \rho v_z T_{\text{O}_2} \end{pmatrix} \quad (12)$$

and

$$\vec{H} = \begin{pmatrix} 0 \\ \mu_t \left( \frac{\partial^2}{\partial r^2} + \frac{\partial^2}{\partial z^2} \right) v_r \\ \mu_t \left( \frac{\partial^2}{\partial r^2} + \frac{\partial^2}{\partial z^2} \right) v_z - \rho g \\ \sigma_s - \sum_n \frac{c_{v_n} D(\rho T_n)}{T_n Dt} + \frac{\partial}{\partial r} \left( \frac{\kappa \partial T}{T \partial r} \right) + \frac{\partial}{\partial z} \left( \frac{\kappa \partial T}{T \partial z} \right) \\ \frac{1}{\tau_{N_2}} (T - T_{N_2}) \\ \frac{1}{\tau_{O_2}} (T - T_{O_2}) \end{pmatrix}. \quad (13)$$

The source-like term  $\vec{C}$  is defined as follows for  $r \neq 0$ :

$$\vec{C}_{r \neq 0} = \frac{1}{r} \begin{pmatrix} \rho v_r \\ \rho v_r^2 + \mu_t \left( \frac{\partial v_r}{\partial r} - \frac{v_r}{r} \right) \\ \rho v_r v_z + \mu_t \frac{\partial v_z}{\partial r} \\ \rho v_r S_{fr} + \frac{\kappa \partial T}{T \partial r} \\ \rho v_r T_{N_2} \\ \rho v_r T_{O_2} \end{pmatrix}. \quad (14a)$$

Equation (14a) is invalid at  $r=0$  due to the  $1/r$  term. However, it can be shown that all terms within the square brackets in Eq. (14a) are identically equal to zero at the origin since, for an axially symmetric model, the radial component of particle velocity is anti-symmetric about  $r=0$  and all other terms are symmetric. Therefore, this term has an indeterminate form  $\vec{C}_{r=0} = \frac{1}{0}(\vec{0})$ , which means that a removable singularity exists at  $r=0$  that can be eliminated through the application of l'Hôpital's rule, yielding

$$\vec{C}_{r=0} = \begin{pmatrix} \frac{\partial}{\partial r}(\rho v_r) \\ 0 \\ \frac{\partial}{\partial r}(\rho v_r v_z) + \mu_t \frac{\partial^2 v_z}{\partial r^2} \\ \frac{\partial}{\partial r} \left( \rho v_r S_{fr} + \frac{\kappa \partial T}{T \partial r} \right) \\ \frac{\partial}{\partial r}(\rho v_r T_{N_2}) \\ \frac{\partial}{\partial r}(\rho v_r T_{O_2}) \end{pmatrix}. \quad (14b)$$

Equation (11), along with the expressions for temperature and pressure [Eqs. (5) and (6)] form a complete set of coupled equations in a form amenable to solution by a finite-difference method. Note that the derivation of this equation set does not rely on an assumption of weak nonlinearity; however, it is assumed that the temperature and pressure fields follow the ideal gas law. To implement the method, the physical model is divided into a grid of cells of dimen-

sion  $dr$  by  $dz$ , each associated with collocated field values, as defined by the matrix  $\vec{F}$ . The spatial grid is discretized such that the dimensions  $dr$  and  $dz$  are significantly smaller than the acoustic wavelength at the maximum frequency of interest; typically, the smallest wavelength is discretized by at least 15 nodes. Spatial derivatives are computed using a seven-point stencil, for sixth order accuracy. The solution is advanced in time using a modified midpoint method (Press *et al.*, 1996), in which centered temporal finite differences are formed over two time steps, which has second order accuracy in time. Each time step is set to a maximum of one-half the Courant stability limit for a 3D grid (Taflove and Hagness, 2000); the factor of one-half is required since temporal differences are computed over two time steps. The method is similar to the "non-staggered leap-frog" procedure used in Ostashev *et al.* (2005) to solve a linear acoustic propagation problem in a windy medium, and also applied by de Groot-Hedlin *et al.* (2010) to solve for infrasound propagation in an absorptive, windy medium.

As described previously, the solution method requires that the code be executed over sufficiently fine spatial and temporal computational grids to capture nonlinear acoustic phenomena up to the highest molecular vibration frequencies, which can range to many kilohertz depending on the atmospheric temperature and humidity. However, the frequencies of interest for infrasound monitoring of explosive shock waves are much lower. Since molecular relaxation losses are the dominant attenuation mechanism up to stratospheric altitudes and thus cannot be neglected, a computationally efficient option for inclusion of vibrational effects is required. An approximation proposed by Pierce (1981, Eq. 10-8.15) is used, which is valid at frequencies that are low compared to the vibration frequency of the  $n$ th-type molecule; the field variables  $\rho T_n$  are removed from the computations and an increment is added to the viscosity to account for molecular relaxation,

$$\mu_t = \mu_t + (\gamma - 1)^2 T \rho_0 \sum_n \frac{c_{v_n}}{\tau_n}, \quad (15)$$

where  $c_{v_n}$  is the specific heat of the  $n$ th-type molecule and the summation is over all molecules for which the low frequency limit holds for the given model discretization. The validity of this approximation stems from the fact that the attenuation due to viscosity is proportional to the square of the frequency, similar to relaxation effects at low frequencies. Pierce (1981) adds the term to the bulk viscosity; however, since attenuation due to shear and bulk viscosity both vary with frequency squared, it can instead be applied to the shear term.

Acoustic sources may be introduced either by inserting time dependent density, velocity, or temperature perturbations at  $r=0$  to synthesize propagation from a continuous source. Alternatively, a spatially distributed mass, velocity, or temperature source with center at  $r=0$  can be used to generate initial perturbations. For solutions initialized with spatially distributed sources, the first time step is computed using forward differences over the first time step and central time differences are used for the remainder of the time steps.

### III. RESULTS

Several solutions to problems of nonlinear propagation through an absorbing atmosphere are presented in this section. The first two examples show results for acoustic propagation through a uniform half-space. The third example involves a spatially distributed thermal source acting upon a model with vertically varying temperature, density, and pressure. For all examples, the bottom boundary is represented by a rigid surface, that is, the algorithm does not include realistic impedance values that would allow for acoustic to seismic coupling.

For examples A and B, the solution is initialized at  $t=0$  by setting the particle velocities  $v_r$  and  $v_z$  to zero, and the vibration temperatures for oxygen and nitrogen to the ambient temperature values. Sources are introduced by adding a density perturbation of the form

$$\rho(r, z) = \begin{cases} A\rho_{\text{sea}}e^{-(R/w)^2}(1 - (R/5w)^2), & R \leq 5w \\ 0, & R \geq 5w \end{cases} \quad (16)$$

to the ambient atmospheric density, where  $\rho_{\text{sea}}$  is the standard sea-level density, equal to  $1.225 \text{ kg/m}^3$  at  $15^\circ\text{C}$ ,  $w$  is the Gaussian half-width, and  $A$  adjusts the amplitude of the source. The source function is thus a truncated Gaussian density perturbation; the truncation factor  $(1 - (R/5w)^2)$ , where  $R = \sqrt{r^2 + (z - z_0)^2}$  serves to initialize the perturbations to zero outside the source region.

Example A demonstrates, first, that the code correctly reduces to a linear solution for a small amplitude source, including the effects of attenuation, and second, that use of the low frequency approximation [Eq. (15)] is an accurate and computationally efficient method of simulating molecular attenuation losses for frequencies well below the molecular vibration frequency. The environmental model consists of a uniform whole space, with ambient density and pressure set to standard sea-level values, an ambient temperature of  $15^\circ\text{C}$ , and 10% relative humidity. For these parameters, the nitrogen and oxygen relaxation frequencies are 65.4 and 2918 Hz, respectively, and the static sound speed is 340.3 m/s. In order to compare attenuation values with those for linear propagation, a small Gaussian density perturbation of the form given by Eq. (16), with half-width  $w=2 \text{ m}$  and amplitude  $A=0.0001$ , is introduced as a source term. Using the relation

$$P = P_0 \left( \frac{\rho}{\rho_0} \right)^\gamma, \quad (17)$$

which may be derived by combining Eqs. (5) and (6) for an isentropic model, where  $P_0=101325 \text{ Pa}$ , the standard sea-level pressure, this mass source is equivalent to a pressure perturbation of 14.2 Pa, or 117 dB re  $20 \mu\text{Pa}$ . Virtual receivers were placed at distances from 10 to 110 m from the source center, at evenly spaced intervals of 10 m. The model was discretized with a node spacing of 0.125 m both radially and vertically, equivalent to 68 nodes per wavelength at a

frequency of 40 Hz, 20 nodes per wavelength at 136 Hz. The temporal discretization was fixed at half the Cauchy stability criterion, 0.1 ms.

An initial test of this code on a model with no attenuation generated the pressure pulses and associated spectra shown in Fig. 1. As indicated, the response to this low amplitude source is approximately linear; that is, the pressure waveforms scale as  $1/r$ , where  $r$  is the distance from the source, but do not vary in shape. Likewise, there is no discernible shift in the frequency content; the spectra vary as  $1/r$  as expected for a spherical source within a whole space.

Results were compared to those for four more models with the following attenuation mechanisms: (1) Nitrogen relaxation only; (2) oxygen relaxation only; (3) classical attenuation only; and (4) all attenuation parameters included. For these models, the bandwidth of the pressure pulses, as shown in Fig. 1(b), straddles the nitrogen relaxation frequency  $f_{\text{N}_2}$ , 65.4 Hz, but is significantly less than the oxygen relaxation frequency  $f_{\text{O}_2}$ , 2918 Hz. A much finer spatial and temporal discretization would be required to accurately model the oxygen vibration temperature in this case. Instead the low frequency approximation, Eq. (15), is used to model oxygen relaxation effects, and the terms involving  $\rho T_{\text{O}_2}$  are dropped from Eq. (11).

The absorption coefficients, in Np/m, are estimated by comparing the amplitude spectra for the attenuated and unattenuated waveforms at two ranges from the source, i.e.,

$$\alpha = -\ln \left( \frac{A(f_{ak})}{A(f_{aj})} \bigg/ \frac{A(f_{ok})}{A(f_{oj})} \right) / (r_k - r_j), \quad (18)$$

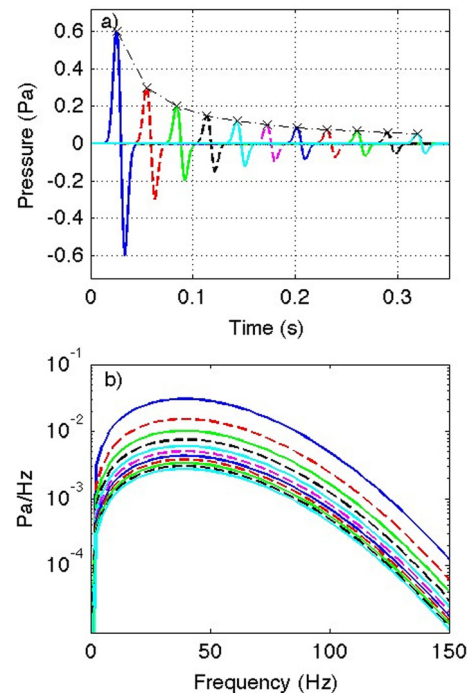


FIG. 1. (Color online) (a) Pressure pulses for a 114 dB Gaussian source with half-width 2 m. The waveforms are shown at ranges of 10–110 m from the source's center, at uniform intervals of 10 m. Every second waveform is plotted with a dashed line. The dashed-dotted line indicates  $1/r$  scaling, where  $r$  is the distance from the source. (b) The associated amplitude spectra.

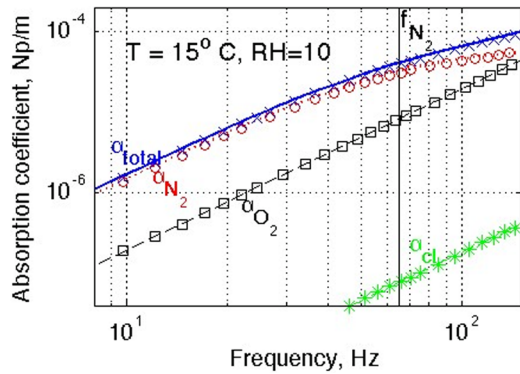


FIG. 2. (Color online) Comparison of theoretical and numerically derived absorption coefficients. The solid line indicates theoretical values for total absorption, the dotted line for nitrogen relaxation, the dashed line for oxygen relaxation, and the dashed-dotted line for classical attenuation. The numerically derived attenuation values are indicated by crosses (total), circles (nitrogen relaxation), squares (oxygen relaxation), and asterisks (classical). The nitrogen relaxation frequency is 65.4 Hz, indicated by the vertical line, and the oxygen relaxation frequency is 2918 Hz.

where  $r_k$  and  $r_j$  are the ranges from the center of the source to virtual receivers  $k$  and  $j$ , respectively,  $A(f_{ok})$  and  $A(f_{oj})$  are the amplitude spectra at receivers  $k$  and  $j$ , respectively, for computations run without attenuation, and  $A(f_{ak})$  and  $A(f_{aj})$  are the corresponding spectra for computations run with attenuation. Figure 2 shows that the numerically derived attenuation values are in agreement with analytic absorption values, derived from Eqs. 10-8.10c and 10-8.11 of Pierce (1981) for linear propagation. The results indicate that the low frequency approximation for molecular relaxation accurately simulates atmospheric absorption well below the molecular vibration frequency for oxygen and into the infrasound frequency bandwidth.

Example B illustrates the effect of changes in the source amplitude on the shape and spectral content of the pressure waveforms as a function of range from the source. The ambient density, pressure and temperature and relative humidity values of this model are identical to those for the previous example. Virtual receivers were placed at ranges from 25 to 500 m from the source center, at evenly spaced intervals of 25 m. Mass sources of the form in Eqs. (14a) and (14b) with  $w = 10$  m were used to initiate each solution. Tests were run for the following cases: (1)  $A = 0.0001$ , for an initial density perturbation of  $0.0001225 \text{ kg/m}^3$ ; (2)  $A = 0.1$ , for an initial density perturbation of  $0.1225 \text{ kg/m}^3$ ; (3)  $A = 0.5$ , for an initial density perturbation of  $.6125 \text{ kg/m}^3$ ; and (4)  $A = 0.8$ , for an initial density perturbation of  $0.98 \text{ kg/m}^3$ . These mass sources are equivalent to pressure perturbations of 117, 177, 192, and 196 dB re  $20 \mu\text{Pa}$ , respectively, derived from Eq. (17). For the largest source, the starting pressure is higher than that of the ambient pressure field. As for example A, the attenuation for oxygen relaxation is handled using the low frequency approximation.

The energy of a mass source is converted into a pressure pulse, as indicated in Fig. 3, which shows the total pressure field solutions at several times for the largest source. Pressure pulses and associated spectra computed for each of these sources are shown in Fig. 4 for virtual receivers from

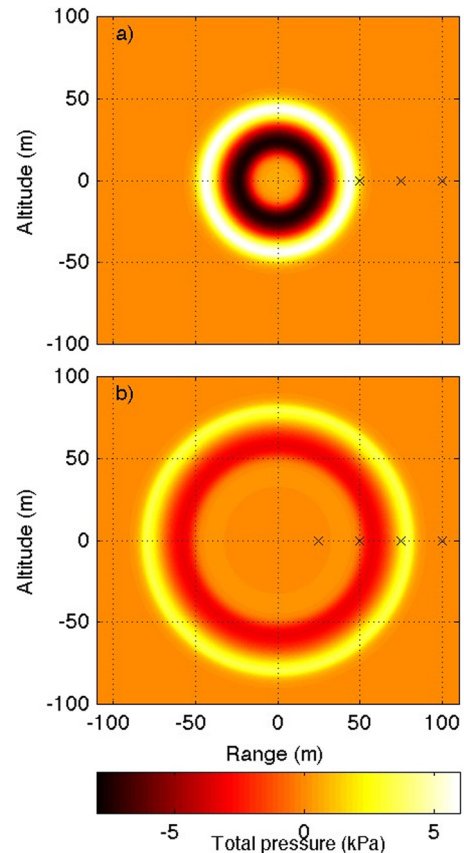


FIG. 3. (Color online) Total pressure field solutions resulting from an initial 196 dB mass source at (a) 0.1 s and (b) 0.2 s. The crosses mark the receiver locations nearest the source. The mass source is converted almost entirely into a blast wave that propagates away from the source region.

50 to 500 m from the source, at intervals of 50 m. As for the previous example, the response to the 117 dB source displays the features of a linear response: The pressure amplitude waveforms scale as  $1/r$ , the positive excursion in pressure is equal in magnitude to the negative excursion that follows, the shape of the pulses does not vary with distance from the source, and there is negligible change in the frequency content of each pulse. This last attribute also indicates that the attenuation is negligible at these frequencies. As indicated in Fig. 2, the attenuation resulting from all loss mechanisms is only on the order of  $6 \times 10^{-6} \text{ Np/m}$  at 20 Hz for linear propagation and is thus not a significant factor at these relatively low frequencies and amplitudes.

The pulse shapes and spectra change as the source amplitude increases. The pressure pulse fronts steepen, as is characteristic of nonlinear acoustic propagation (Lighthill, 1978; Pierce, 1981) and the trailing negative excursion in pressure decreases in magnitude with respect to the positive excursion. The corresponding amplitude spectra indicate a shift in frequency content from lower to higher frequencies for larger sources, along with the increased frequency scalloping associated with wavefront steepening. For the 177 dB source ( $A = 0.1$ ), Fig. 4(d) shows that the amplitude spectra are shifted toward higher frequencies than for the smaller source, but there is little further shifting in the amplitude spectra at distances beyond about to 250–300 m, once the peak pulse pressure decreases to just over 100 Pa. Since the

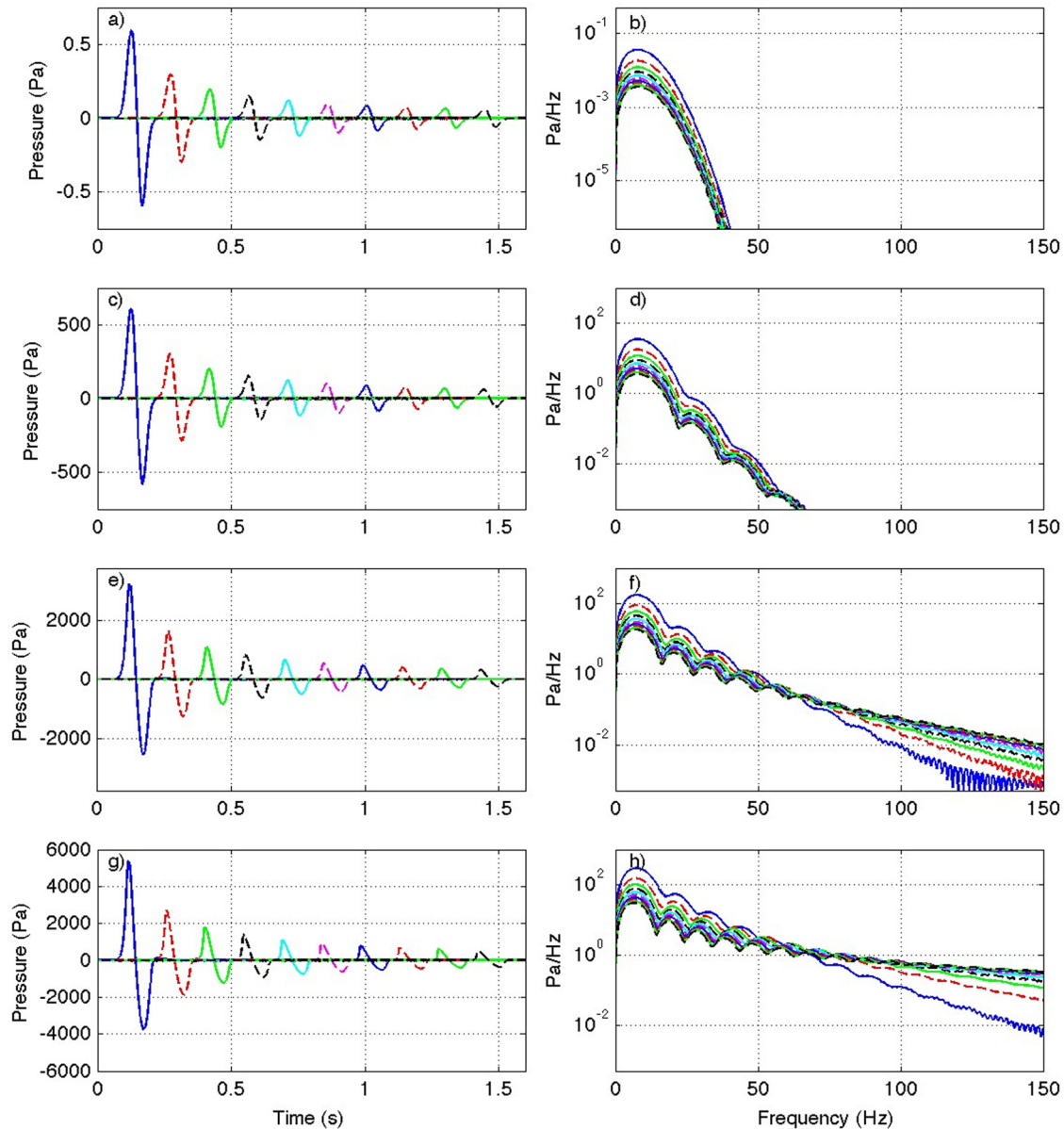


FIG. 4. (Color online) Pressure pulses and associated amplitude spectra for sources of varying amplitude within a whole-space model, shown at virtual receiver places at ranges of 50–500 m from the center of the source, at intervals of 50 m. (a) Waveforms for a 117 dB source and (b) associated spectra; (c) waveforms for a 177 dB source and (d) associated spectra; (e) waveforms for a 192 dB source and (f) associated spectra; (g) waveforms for a 196 dB source and (h) associated spectra. As the source amplitudes increase, the waveforms become increasing saw-toothed and the spectral content shifts from lower to higher frequencies.

shape of a waveform and its spectrum remain unchanged for linear propagation, this suggests that propagation may be treated as linear once the acoustic pressure perturbations drop to about 0.1% of ambient values. Note that the scalloping observed in Figs. 4(f) and 4(h) may be an artifact of model discretization; however, there has been no analysis of numerical dispersion for the nonlinear acoustic propagation case as there has for the linear case (de Groot-Hedlin, 2008; de Groot-Hedlin *et al.*, 2010). Such an analysis is beyond the scope of this paper.

The difference in magnitude between the peak positive and negative pulses for larger sources suggests that pulse amplitudes, defined as the difference between maximum and minimum recorded pressure, do not scale simply with source amplitude. Figure 5 shows the variation in pulse amplitude

with range from the source for each mass source, scaled by the maximum source pressure. The pressure decreases by  $1/r$  for the smallest source modeled, as expected for a linear source. If propagation were linear for all source amplitudes, the pulse amplitudes vs range would all fall along the same line. However, the nonlinear propagation results show that pulse amplitudes do not scale linearly with the source pressure; instead, for large sources, a doubling of source pressure yields less than twice the pulse amplitude. For instance, the largest source, at 196 dB, is approximately 9000 times larger than the smallest, at 117 dB, but the pulse pressures from the largest source are only about 7700 times larger than for the smallest.

The effect of nonlinear propagation on acoustic waveforms is examined further in Fig. 6. Figure 6(a) shows the

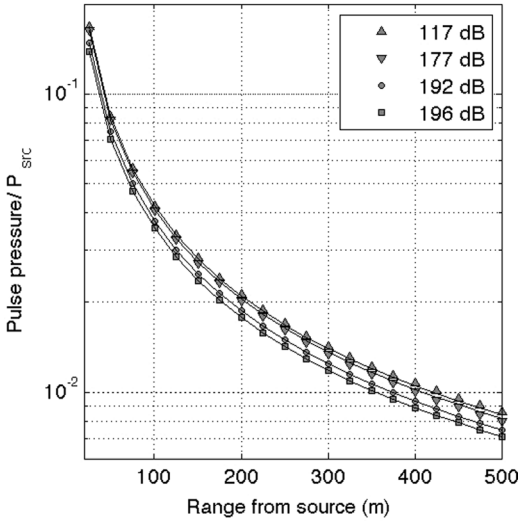


FIG. 5. (a) Normalized pulse pressure vs range product for the 117 dB source, the 177 dB source, the 192 dB source, and the 196 dB source. The pulse pressure is scaled by the source pressure perturbation. For linear propagation, all values would lie along the same  $1/r$  line.

differential velocities as a function of range for each source. Differential velocities are computed from the travel times associated with the maximum pulse amplitude at each receiver. As shown, high amplitude pressure pulses are associated with higher sound speeds. As the pulse propagates away from the source, the sound speeds revert to the value for the whole space, 340.5 m/s. Figure 6(b) shows the dominant frequency for each waveform as a function of range from the source. Since nonlinear propagation results in a shift from

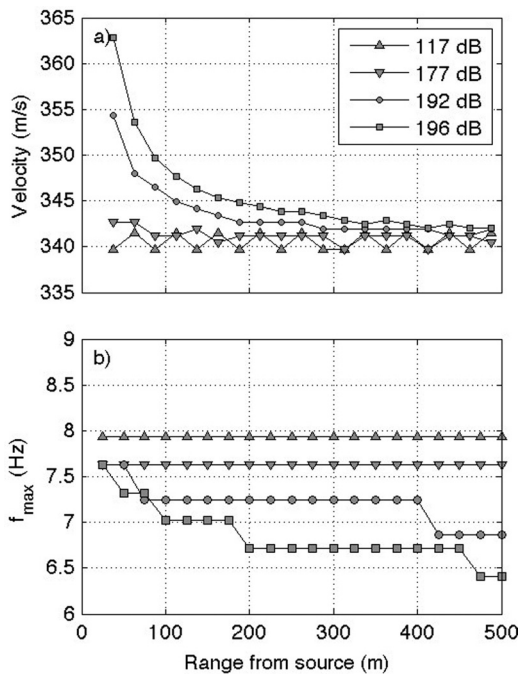


FIG. 6. (a) Differential sound speeds, based on travel times between amplitude maxima at each virtual receiver. The variations in differential velocity for the smallest source are due to discretization error. The sound speed for the whole space is 340.5 m/s. (b) Dominant frequency for each waveform. The values vary unevenly due to the temporal and spatial discretization used in the computations.

low to high frequencies, the dominant frequency decreases with range from the source; this effect is more pronounced for large sources.

Example C is most directly applicable to studies of the propagation of infrasound generated by atmospheric explosions through realistic temperature, pressure, and density models of the atmosphere. Tests were run for the following environmental models: (1) A half-space model with a temperature of  $15^\circ\text{C}$  and standard sea-level pressure; (2) a model with a uniform temperature of  $15^\circ\text{C}$ , (3) a model with a surface temperature of  $15^\circ\text{C}$  and a negative temperature gradient of  $6.5^\circ\text{C}/\text{km}$  up to 11 km; and (4) a model with a surface temperature of  $15^\circ\text{C}$  and a positive temperature gradient of  $6.5^\circ\text{C}/\text{km}$  up to 11 km. For the last three environmental models, the pressure varies hydrostatically and the ambient atmospheric density is derived from the pressure and temperature profiles using the ideal gas law. The models are terminated below by a rigid surface. The temperature and density profiles for each of these models are shown in Fig. 7. The model with a lapse rate of  $-6.5^\circ\text{C}/\text{km}$  up to 11 km, with constant temperature above, is the model that most closely resembles the International Standard Atmosphere model. For this model, the decrease in temperature, and hence sound speeds, with altitude causes upward refraction of sound at some distance from the source, creating a shadow zone where little acoustic energy can penetrate.

In general, explosions may be modeled as a combination of mass, velocity, or thermal fields, depending on the type of explosion. For this example the solution is initialized at  $t = 0$  with a pure thermal source, i.e., sources are introduced by adding a temperature perturbation of the form

$$T_{\text{pert}}(r, z) = \begin{cases} T_A e^{-(R/w)^2} (1 - (R/4w)^2), & R \leq 4w \\ 0, & R \geq 4w \end{cases} \quad (19)$$

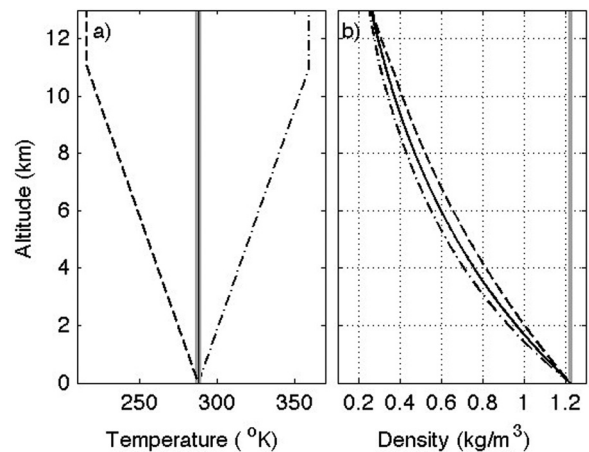


FIG. 7. (a) Temperature and (b) density profiles for the final set of models. Model 1 (thick gray lines) is a half-space with uniform temperature of  $15^\circ\text{C}$  and standard sea-level pressure. The pressure in the remainder of the models varies hydrostatically, and thus decreases exponentially as  $e^{-g_0 z / R_0 T(z)}$ . Model 2 (thin black lines) has a uniform temperature of  $15^\circ\text{C}$ . Model 3 (dashed lines) has a negative temperature gradient of  $6.5^\circ\text{C}/\text{km}$  up to 11 km. Model 4 (dashed-dotted lines) has a positive temperature gradient of  $6.5^\circ\text{C}/\text{km}$  up to 11 km.

to ambient temperature values. The Gaussian half-width  $w$  is set to 400 m, resulting in peak frequencies of about 0.2 Hz, well into the infrasound frequency range. The maximum anomalous temperature  $T_A$  is set to 200 °C, which leads to a maximum pressure perturbation of 191 dB re 20  $\mu$ Pa at the source. The starting particle velocities  $v_r$  and  $v_z$  are set to zero, and the density profiles are set to the ambient atmospheric value. For this example, the molecular vibration frequencies are much higher than the frequencies of interest, therefore the attenuation due to both nitrogen and oxygen relaxation processes is handled by combining their effects with the shear viscosity using Eq. (15). The source center is set to 6 km altitude, where the atmospheric pressure is approximately half that on the ground for the models with variable pressure. Virtual receivers were placed on the rigid surface at ranges from 0 km, directly below the source, to 46 km from the source, at even intervals of 1 km.

For solutions initialized by a mass source, virtually all of the energy is directed into an acoustic wave (cf. Fig. 3). However for thermal sources, only a portion of the energy is directed into a blast wave with the remainder left behind as a high temperature/low density anomaly. The characteristics of a thermal source are examined further in Figs. 8 and 9. Figure 8 shows the total pressure field and overpressure near the source at times  $T = 5.2$  s,  $T = 13$  s, and  $T = 20.8$  s, for the

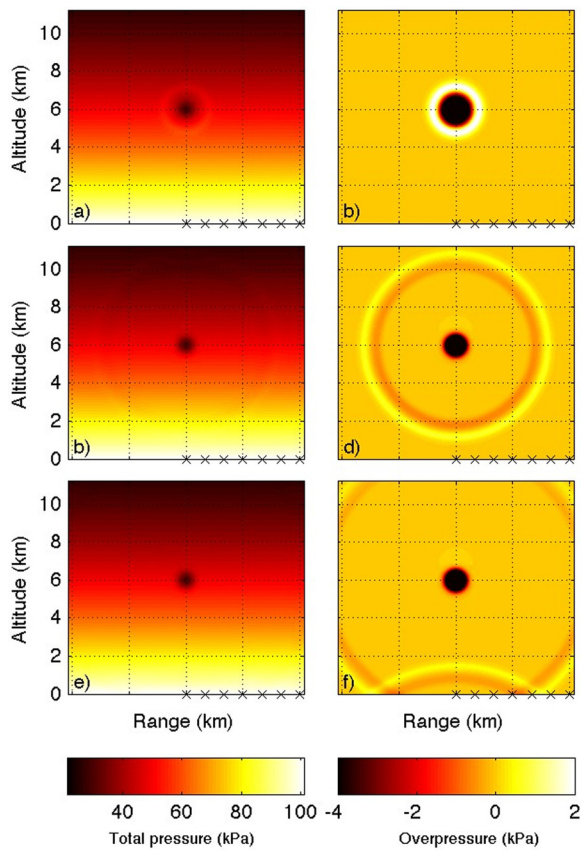


FIG. 8. (Color online) Total pressure field solutions resulting from an initial 200 °C thermal source at times (a) 5.2 s, (c) 13 s, and (e) 20.8 s for model 2 (cf. Fig. 7). The corresponding overpressure (total pressure – ambient pressure) is shown in (b), (d), and (f). The crosses mark the receiver locations on the rigid surface nearest the source. The solution at  $T = 20.8$  s was included to show a reflection at the rigid boundary.

model with uniform temperature and hydrostatically varying pressure (model 2). A part of the thermal energy is converted to a blast wave that propagates away from the source, leaving behind a residual pressure perturbation near the source region. Figure 9 shows the density and velocity fields in the source region at 5.2 s [Fig. 9(a)], showing the acoustic wave propagating from the source and the remaining low density perturbation, and at 13 s [Fig. 9(b)], by which time the blast wave has propagated further from the source region. The negative density perturbation remaining near the source moves upward due to buoyancy. This is the initial, upward movement of a gravity wave generated by the thermal source and demonstrates the capability of the code to compute all realistic pressure, density, and temperature disturbances that result from a given source, rather than solely the acoustic perturbations.

The change in pulse amplitude with range from the source is shown in Fig. 10 for each model. The pulse amplitudes vary approximately as  $1/r$  for all models within about 20 km from the source; at greater distances the amplitudes drop off more rapidly for the model with the negative temperature gradient, indicating decreased acoustic penetration

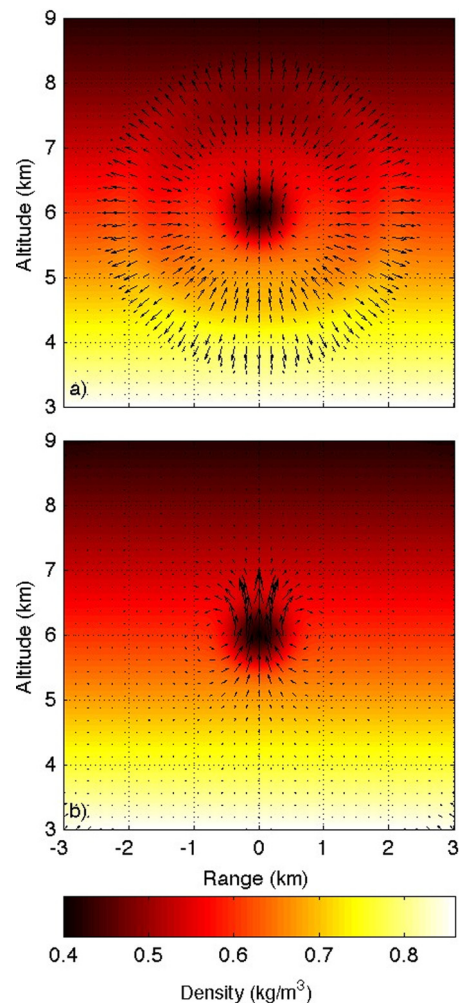


FIG. 9. (Color online) Total density field solutions resulting from an initial 200 °C thermal source at times (a) 5.2 s and (b) 13 s for model 2 (cf. Fig. 7). Arrows indicate the particle velocities. The thermal source leaves a low density residual near the source region.

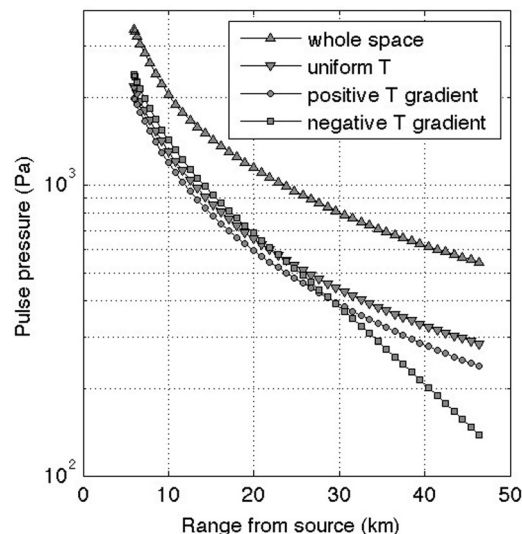


FIG. 10. Pulse amplitudes vs range for models with varying ambient temperature and density fields as shown in Fig. 7.

into the shadow zone. Figure 10 also shows that the pulse pressure associated with the half-space model is significantly larger than for the models with hydrostatically varying pressure. This suggests that the pulse pressure generated by an explosion is strongly dependent on its altitude. The results also indicate that variability in ambient temperature and pressure has a strong bearing on pulse amplitudes recorded at receivers, and cannot be neglected in the development of source yield relationships.

#### IV. CONCLUSIONS

A computationally efficient method of synthesizing the propagation of infrasound energy released by very large explosions through realistic representations of the atmosphere has been presented. By restricting the source and atmospheric models to be axially symmetric, the solution of a set of nonlinear fluid dynamic equations in cylindrical coordinates allows for computations in 2D. The inclusion of gravitational effects and low frequency approximations to molecular vibration losses allow not only for the accurate computation of acoustic phenomena to very low frequencies, but also other types of pressure, density, and temperature disturbances excited by very large sources, including gravity waves.

The results indicate the recorded infrasound pulse pressure does not scale in direct proportion to the source amplitude, as it would for linear propagation. Instead, the pressure pulses for large sources are lower than for the corresponding linear case due to the shift in energy from low to high frequencies, where attenuation is enhanced. The results also indicate that nonlinear infrasound amplitudes depend strongly on atmospheric temperature and pressure variations, as is the case for linear propagation.

The algorithm presented here has application to the development of source yield relationships. However, more work on the code is needed to deal with blast wave sources, which would have much steeper initial rise times than for the

sources presented here. Improvements in the code to allow for the effects of winds would further aid in accurate synthesis of infrasound propagation through realistic models of the atmosphere. However, given that infrasound amplitudes are highly dependent upon atmospheric variability, the estimation of energy released by explosions is likely to be a highly non-unique problem unless the event is viewed by a sufficient number of infrasound sensors, and accurate atmospheric models are available.

Possible extensions of this work involve using the algorithm to investigate infrasound propagation from a wide range of source types. In this paper, mass sources and thermal sources were used to initialize solutions although, in general, sources are not purely mass sources or thermal sources, or velocity sources. Each type of explosion, e.g., nuclear, chemical, or even explosive volcanic eruptions, is associated with different source properties. For instance, a volcanic explosion is accompanied by a rapid expansion of gases, which could be modeled as a combination of mass and velocity sources; a chemical explosion is accompanied by a rapid release of hot gases, which might be modeled as a thermal source. A full exploration of the different combinations of density, velocity, or thermal field values that may be used to initialize a solution is beyond the scope of this paper. However, the code is sufficiently flexible to allow any combination of mass, thermal, or velocity sources, to allow for investigation of different initial solutions on shock wave propagation. This suggests that the code might be used in the future to compute the partitioning of energy from explosions into shock waves vs gravity waves, turbulent vortices or other perturbations to atmospheric flow more commonly associated with the weather.

Another possible extension is to use the code to model nonlinear effects as infrasound propagates to high altitudes. Atmospheric pressure decreases exponentially with altitude, with a halving distance of approximately 6 km, so that pressure perturbations associated with upward-propagating acoustic energy may become a significant fraction of ambient pressure, resulting in nonlinear propagation (Bass *et al.*, 2006). Thus, nonlinear effects may significantly alter infrasound returns from the stratosphere or thermosphere, even for sources of moderate size.

#### ACKNOWLEDGMENTS

The author thanks Dr. Rodney Whitaker and an anonymous reviewer for their constructive comments.

- Bass, H., Bhattacharyya, J., Garcés, M., Hedlin, M., Olson, J., and Woodward, R. (2006). "Infrasound," *Acoust. Today* 2, 9–19.
- Bhattacharyya, J., Bass, H. A., Drob, D. P., Whitaker, R. W., ReVelle, D. O., and Sandoval, T. D. (2003). "Description and analysis of infrasound and seismic signals recorded from the Watusi explosive experiment, September 2002," *Proceedings of the 25th Seismic Research Review*, pp. 587–596.
- Christie, D. R., and Campus, P. (2010). "The IMS infrasound network: Design and establishment of infrasound stations," in *Infrasound Monitoring for Atmospheric Studies*, edited by A. Le Pichon, E. Blanc, and A. Hauchecorne (Springer, New York), Chap. 2, pp. 29–75.
- de Groot-Hedlin, C., Hedlin, M., and Walker, K. (2011). "Finite difference synthesis of infrasound propagation through a windy, viscous atmosphere:

- Application to a bolide explosion detected by seismic networks,” *Geophys. J. Int.* **185**, 305–320.
- de Groot-Hedlin, C. D. (2008). “Finite-difference time-domain synthesis of infrasound propagation through an absorbing atmosphere,” *J. Acoust. Soc. Am.* **124**, 1430–1441.
- Del Pino, S., Després, B., Havé, P., Jourden, H., and Piserchia, P. (2009). “3D finite volume simulation of acoustic waves in the Earth atmosphere,” *Comput. Fluids* **38**, 765–777.
- Drob, D. P., Picone, J. M., and Garcés, M. A. (2003). “The global morphology of infrasound propagation,” *J. Geophys. Res.* **108**, 4680, doi:10.1029/2002JD003307.
- Edwards, W. N., Brown, P. G., and ReVelle, D. O. (2004). “Bolide energy estimated from infrasonic measurements,” *Earth, Moon, Planets* **95**, 501–512.
- Edwards, W. N., Brown, P. G., and ReVelle, D. O. (2006). “Estimates of meteoroid kinetic energies from observations of infasonic airwaves,” *J. Atmos. Sol.-Terr. Phys.* **68**, 1136–1160.
- Evers, L. G., and Haak, H. W. (2010). “The characteristics of infrasound, its propagation and some early history,” in *Infrasound Monitoring for Atmospheric Studies*, edited by A. Le Pichon, E. Blanc, and A. Hauchecorne (Springer, New York), Chap. 1, pp. 3–27.
- Gainville, O., Blanc-Benon, P., Blanc, E., Roche, R., Millet, C., Le Piver, F., Despres, B., and Piserchia, P. F. (2010). “Misty Picture: A unique experiment for the interpretation of the infrasound propagation from large explosive sources,” in *Infrasound Monitoring for Atmospheric Studies*, edited by A. Le Pichon, E. Blanc, and A. Hauchecorne (Springer, New York), Chap. 18, pp. 575–598.
- Landau, L. D., and Lifshitz, E. M. (1959). *Fluid Mechanics*, 2nd ed. (Elsevier, Burlington, MA), pp. 1–539.
- Le Pichon, A., Antier, K., Hernandez, B., Minaya, E., Burgon, B., Drob, D., Evers, L. G., and Vaubaillon, J. (2008). “Evidence for a meteoritic origin of the September 15, 2007, Carancas crater,” *Meteorit. Planet. Sci.* **43**, 1797–1809.
- Lighthill, J. (1978). *Waves in Fluids* (Cambridge Mathematical Library, Cambridge, UK), pp. 144–165.
- Lingevitch, J. F., Collins, M. D., and Seigmann, W. L. (1999). “Parabolic equation for gravity and acousto-gravity waves,” *J. Acoust. Soc. Am.* **105**, 3029–3056.
- Marsden, O., Vayno, L., Boger, C., and Bailly, C. (2008). “Study of long-range infrasound propagation with high-performance numerical schemes applied to the Euler equations,” *13th Long Range Sound Propagation Symposium*, October 16–17, Lyon, France, pp. 201–216.
- Mutschlecner, J. P., and Whitaker, R. W. (2010). “Some atmospheric effects on infrasound signal amplitudes,” in *Infrasound Monitoring for Atmospheric Studies*, edited by A. Le Pichon, E. Blanc, and A. Hauchecorne (Springer, New York), Chap. 14, pp. 455–474.
- Ostashev, V. E., Wilson, D. K., Liu, L., Aldridge, D. F., Symons, N. P., and Marlin, D. (2005). “Equations for finite-difference, time-domain simulation of sound propagation in moving inhomogeneous media and numerical implementation,” *J. Acoust. Soc. Am.* **117**, 503–517.
- Pierce, A. D. (1981). *Acoustics: An Introduction to its Physical Principles and Applications*, (Acoustical Society of America, Woodbury, NY), pp. 1–678.
- Press, W. H., Teukolsky, S. A., Vetterling, W. T., and Flannery, B. P. (1996). *Numerical Recipes in Fortran77*, 2nd ed. (Cambridge University Press, New York), pp. 716–718.
- Shepherd, M. R., Gee, K. L., and Wochner, M. S. (2009). “Short-range shock formation and coalescence in numerical simulation of broadband noise propagation,” *J. Acoust. Soc. Am.* **126**, 2886–2893.
- Sutherland, L. C., and Bass, H. E. (2004). “Atmospheric absorption in the atmosphere up to 160 km,” *J. Acoust. Soc. Am.* **115**, 1012–1032.
- Taflove, A., and Hagness, S. C. (2000). *Computational Electrodynamics: The Finite-Difference Time-Domain Method*, 2nd ed. (Artech House, Norwood, MA), Chap. 4, pp. 109–174.
- Whitaker, R. W., Sandoval, T. D., and Mutschlecner, J. P. (2003). “Recent infrasound analysis,” *Proceedings of the 25th Seismic Research Review*, pp. 646–653.
- Wochner, M. S., Atchley, A. A., and Sparrow, V. W. (2005). “Numerical simulation of finite amplitude wave propagation in air using a realistic atmospheric absorption model,” *J. Acoust. Soc. Am.* **118**, 2891–2898.